# Using Correlation Integrals to Characterize 3D Stellar Orbits

# Eric I. Barnes

Department of Physics & Astronomy, Louisiana State University, Baton Rouge, LA 70803 barnes@physics.lsu.edu

# **ABSTRACT**

In an effort to more fully understand the variety of stellar distribution functions that can be used to construct models of realistic galaxies, the correlation integral method for orbit characterization that previously has been introduced by Grassberger & Procaccia (1983a) and Carnevali & Santangelo (1984) is examined in considerable detail. The broad utility of the method is validated and demonstrated by applying it to orbits in a number of different, previously studied test cases (1D, 2D, and 3D; nonrotating and rotating). At the same time, the correlation integral method is compared and contrasted with other more traditional characterization tools such as Lyapunov exponents and surfaces of section. The method is then extended to orbits in a previously unexamined rotating, 3D bar potential. The correlation integral method is found to be a simple and reliable way to quantitatively categorize orbits in virtually any potential. It is recommended that it be broadly adopted as a tool for characterizing the properties of orbits and, by extension, stellar distribution functions, in all Hamiltonian dynamical systems.

# 1. Introduction

### 1.1. Background

The study of orbits in three-dimensional (3D) gravitational potentials is of broad astrophysical interest. Whether the orbits under investigation are those of asteroids in the solar system (e.g., Pilat-Lohinger et al. 1999), stars in a globular cluster or a galaxy (e.g., Carpintero et al. 1999), or galaxies in a cosmological simulation (e.g., Colpi et al. 1999), methods of characterizing the orbits can be extremely useful, especially when an attempt is made to understand what the "typical" behavior is of a very large collection of orbits in a particular physical system. These methods, some of which are discussed below in §3, are most useful when they are quantitative, reliable, and applicable to a wide variety of systems.

Here, the analysis will focus on stellar orbits in models of time-invariant galactic potentials. With this in mind, a brief review of some basics of stellar dynamics is presented. Stars in galaxies are presumed to form a collisionless system, that is, the forces felt by any one star are due only to the mean forces produced by all other stars. The distribution function, f, of stars must therefore sat-

isfy the collisionless Boltzmann equation (Binney & Tremaine 1987),

$$\frac{df}{dt} = \frac{\partial f}{\partial t} + \sum_{i} \frac{\partial f}{\partial w_i} \dot{w}_i = 0, \tag{1}$$

where the  $w_i$  are the phase space coordinates, e.g.,  $(x, y, z, \dot{x}, \dot{y}, \dot{z})$ . A by-product of this equation is that any time-independent function of phase space coordinates, known as an integral of motion, must be a valid solution of eq. (1). This fact is incorporated into the Jeans Theorem: any steady-state solution of eq. (1) must be a function of integrals of motion and any function of integrals of motion must likewise solve eq. (1) (Binney & Tremaine 1987). A stronger, qualified statement can be made. If all orbits in a given potential are regular then any solution to eq. (1) is a function of three integrals of motion. This is known as

<sup>&</sup>lt;sup>1</sup>We use the term "regular" to describe orbits that respect a number of isolating integrals of motion that is greater than or equal to the degrees of freedom of the orbit (Binney & Tremaine 1987). For example, an orbit in a 2D potential must have at least two isolating integrals in order to be considered regular. On the other hand, we use "quasi-ergodic" as a blanket term for both stochastic and semistochastic orbits; irregular orbits are fully ergodic. Ergodic and quasi-ergodic orbits respect only one complete

the Strong Jeans Theorem (Binney & Tremaine 1987). Indeed, in potentials that have analytically prescriptible integrals of motion, such as spherical or axisymmetric systems, a variety of distribution functions have been investigated (e.g., King 1966; Kalnajs 1976).

However, most realistic models of galaxies are not as simple as those discussed above, and different tactics must be used to investigate the properties of the stellar distribution functions that are associated with these more realistic systems. And while an in-depth discussion of the creation of such models is beyond the scope of this paper, a short overview is given here. N-body simulations (e.g., Miller & Smith 1979; Hohl & Zang 1979; Combes & Sanders 1981; Miller et al. 1982; Pfenniger & Friedli 1991) have been widely used to generate stellar distribution functions for steadystate galaxy models. By design, many of these simulations have begun with axisymmetric distributions of point particles, then the dynamical systems quickly deform to bar-shaped objects. Most of these studies have focused on the global evolution of the bar, but some (Miller & Smith 1979; Pfenniger & Friedli 1991) have also looked at constituent orbits of the bars and have found evidence for nonanalytical integrals of motion. Performing numerical integrations of individual orbits in analytical potentials provides further evidence for these nonanalytical integrals in studies designed to find periodic orbits (e.g., Heisler et al. 1982; Magnenat 1982; Mulder & Hooimeyer 1984; Pfenniger 1984; Martinet & de Zeeuw 1988; Hasan et al. 1993). Uncovering periodic orbits has been very important in the context of studies of 3D galaxy models because Schwarzschild (1979, 1982) developed procedures for creating self-consistent potential-density pairs (and associated steady-state distribution functions) once the periodic orbits for a given 3D potential are known. These techniques have been extended to model realistic stellar dynamical systems (e.g., Rix et al. 1997; van der Marel et al. 1998; Cretton et al. 1999; Cretton, Rix, & de Zeeuw 2000).

While the importance of regular orbits has been the focus of many stellar dynamics research projects, the importance and likely existence of quasi-ergodic orbits in realistic galaxy

isolating integral of motion, either the specific energy,  $\epsilon$ , or the Jacobi constant,  $\epsilon_J$ .

potentials also has been discussed (Goodman & Schwarzschild 1981; Binney 1982b; Habib et al. 1997; Valluri & Merritt 1998). While the previously mentioned studies involved analytical potentials, Barnes & Tohline (2001) have also found that quasi-ergodic stellar orbits are quite common in a numerically-created, gaseous bar. Quasi-ergodic orbits also appear in N-body simulations of galactic bars (see, for example, Sparke & Sellwood 1987). A specific example of a situation in which quasi-ergodic orbits play an important role is in galaxy models with massive central objects (e.g., Udry & Pfenniger 1988, Valluri & Merritt 1998). In a detailed analysis of the influence that massive central objects have on stellar orbits, Gerhard & Binney (1985) suggest that sufficiently massive central objects will scatter into quasi-ergodic orbits trajectories that initially: 1) are regular; 2) pass near the central object; and 3) support nonaxisymmetric distributions, such as bars. With the current interest in understanding active galactic nuclei as well as the recent discovery of a link between the masses of central objects and central stellar velocity dispersions (Ferrarese & Merritt 2000; Gebhardt et al. 2000a), more accurate modeling of the distribution functions of such systems (along the lines of van der Marel et al. 1998) could provide some insight into the observational evidence.

In an effort to better characterize orbits (both regular and quasi-ergodic) in astrophysically interesting potentials, the relative utility of the correlation integral method has been examined. As pointed out by Grassberger & Procaccia (1983a) and Carnevali & Santangelo (1984), the correlation integral method is a flexible and accurate characterization technique that has been widely utilized by physicists but has been virtually ignored by the stellar dynamical community. This technique distinguishes orbits based on the number of isolating integrals of motion that are respected by any given orbit. This makes it a useful, quantitative tool for examining stellar distribution functions that would arise in potentials such as the ones mentioned above. Regular and nonregular orbits can be differentiated. Within the regular class, periodic and quasi-periodic orbits can also be distinguished from one another. Additionally, this technique can distinguish between 3D orbits that respect two isolating integrals and those that respect only one. This ability to distinguish in a clear and quantitative fashion between various types of orbits makes the correlation integral method particularly well suited to involvement in studies of 3D potentials where quasi-ergodic orbits are likely to play an important role. The primary objective of this paper is to demonstrate the quantitative reliability and broad utility of the correlation integral method by applying it as a characterization tool to orbits in a wide variety of potentials – most of which are familiar to the stellar dynamics community – and by comparing and contrasting it to other techniques that have been broadly used to characterize orbits. This will place the community in a position to effectively utilize this tool in a wide variety of problems.

The remainder of this paper is divided as follows. The different models (one map and several potentials) are introduced individually in §2. Section 3 contains summaries of the numerical integration technique and various orbital characterization methods that are utilized in this study. Tests of and results acquired with the correlation integral method are presented in §4. Also discussed in this section are the results from a previously unexamined 3D potential. Finally, §5 presents a summary of the findings.

## 2. Models

In order to illustrate the basic utility of the correlation integral method, as well as the accuracy of this particular implementation of the method, several systems that previously have been well studied and characterized using other techniques are presented.

### 2.1. Hénon Map

The simplest system to attack using the correlation integral method is one that can be contained in a 2D phase space. The Hénon map is one such system that exhibits nontrivial behavior. It is prescribed by the following set of iterative equations (Hénon 1976):

$$x_{i+1} = y_i + 1 - ax_i^2, (2)$$

and

$$y_{i+1} = bx_i, (3)$$

where a and b are constants. Rather than solving a pair of coupled differential equations for position and velocity, phase space is occupied by choosing initial x and y values, then iterating back and forth between these two algebraic expressions. When a=1.4 and b=0.3, the Hénon map has a strange attractor in phase space, that is, the dimensionality of occupied phase space is noninteger (fractal).

#### 2.2. Richstone Potential

Following the lead of Carnevali & Santangelo (1984), orbits in the scale-free, logarithmic potential referred to here as the Richstone potential (Richstone 1980, 1982) are also studied. (A triaxial version of this potential has been studied in Binney 1981 and is known as Binney's potential.) One nice feature of this potential is that it can be used to study either 2D or 3D orbits (4D and 6D phase spaces, respectively). To investigate fully 3D orbits, the following form of the potential is utilized.

$$\Phi_{\rm R}(x,y,z) = \frac{v_0^2}{2} \ln \left( x^2 + y^2 + \frac{z^2}{q^2} + R_c^2 \right), \quad (4)$$

where  $v_0$  is the constant circular speed for the potential, q is a measure of the flattening of the potential, and  $R_c$  is a core radius. There are three possible potential shapes:

- q > 1 the potential is prolate spheroidal;
- q = 1 the potential is spherical;
- q < 1 the potential is oblate spheroidal.

As in Richstone (1982), the parameters are set as q = 0.75 and  $R_c = 0.1$ .

In order to examine 2D orbital motion in the Richstone potential, thereby reducing the analysis from a 6D to a 4D phase space, first transform eq.(4) to cylindrical coordinates  $(R, \phi, z)$ . It is clear that  $\Phi_{\rm R}$  is axisymmetric, so the Lagrangian is cyclic in  $\phi$ , which means that the z-component of angular momentum is constant. With this restriction, orbits in the 2D Richstone potential move under the influence of the following effective potential,

$$\Phi_{\rm R,eff}(R,z) = \frac{v_0^2}{2} \ln \left( R^2 + \frac{z^2}{q^2} + R_c^2 \right) + \frac{L_z^2}{2R^2}.$$
 (5)

It is this 2D potential that Carnevali & Santangelo (1984) used to validate their implementation of the correlation integral method.

### 2.3. Hénon-Heiles Potential

The Hénon-Heiles potential (Hénon & Heiles 1964) is a well-known potential that supports both regular and quasi-ergodic orbits. This potential has the form,

$$\Phi_{\rm HH}(R,z) = \frac{1}{2}(R^2 + z^2 + 2R^2z - \frac{2}{3}z^3).$$
 (6)

For energies  $\epsilon \lesssim 0.01$ , almost all orbits in this potential are regular. As the energy is increased, more and more of phase space is occupied by quasiergodic orbits. At an energy  $\epsilon = 1/6$ , the situation is reversed in that most orbits are quasi-ergodic.

### 2.4. Stäckel Potential

Since Stäckel potentials are separable, all orbits in such potentials are regular. This feature makes orbits in Stäckel potentials ideal subjects for testing characterization techniques. The Stäckel potential that is used in this study has the form (de Zeeuw & Lynden-Bell 1985),

$$\Phi_{\rm S} = \frac{-v_0^2}{1 + (\frac{x}{a})^2 + (\frac{y}{b})^2 + (\frac{z}{c})^2},\tag{7}$$

where  $v_0 = 1.0$ , a = 1.0, b = 0.8, and c = 0.6. This is a triaxial potential where the minor axis lies along the z-axis, the intermediate axis lies along the y-axis, and the major axis lies along the x-axis.

### 2.5. Cazes Bar Potential

In an effort to investigate the fission hypothesis for binary star formation, Cazes (1999) has produced two models of rapidly rotating, steady-state, triaxial, gaseous density distributions using a numerical hydrodynamics code. These models have compressible (n=3/2) polytropic equations of state and nontrivial internal flows, including two relatively weak standing shocks. A detailed description of these models appears in Cazes & Tohline (2000). The hydrodynamics simulation

that created these models was performed with dimensionless units. This allows the results to be scaled to a variety of systems simply by choosing an appropriate mass and length scale (Williams & Tohline 1987). For example, choosing a mass of  $1.0\,M_\odot$  and a length scale  $R_{\rm eq}\approx 4.57\,{\rm AU}$  describes a protostellar object of density  $\rho\approx 10^{-9}\,{\rm g\,cm^{-3}}$  (Cazes 1999). Alternatively, for a mass of  $10^{10}\,M_\odot$  and length scale  $R_{\rm eq}\approx 2\,{\rm kpc}$ , the now galactic-sized object has a density  $\rho\approx 10^{-23}\,{\rm g\,cm^{-3}}$ . With this galactic scaling in mind, the Cazes & Tohline (2000) "Model B" is adopted as an example of a nontrivial, rotating, bar-like structure with a self-consistent and realistic potential-density pair. Hereafter, this model will be referred to as the "Cazes bar."

Since the Cazes bar was created numerically, values of various quantities such as mass density and the gravitational potential are specified at discrete locations on a computational grid; specifically, Cazes & Tohline (2000) used a  $128\times64\times256$  cylindrical  $(R,z,\phi)$  grid. For reasons that will be made clear in a later section, it is difficult to accurately evaluate Lyapunov exponents and the correlation integral on such a coarse, discrete grid. In analyzing orbits in the Cazes bar potential, an analytical potential constructed along the lines discussed in Barnes & Tohline (2001) to closely resemble the numerical Cazes bar potential will be adopted instead. Specifically, the following analytical potential will be used:

$$\Phi_{\text{aCB}}(x, y, z) = N \left\{ 1 - \left( 1 + \left( \frac{x}{R_{\text{L}2}} \right)^{\alpha} + \left( \frac{y}{qR_{\text{L}2}} \right)^{2} + \left( \frac{z}{q_{z}z_{\text{lim}}} \right)^{\gamma} \right)^{-\beta} \right\}$$

$$- \frac{1}{2}\Omega^{2}(x^{2} + y^{2}) + \Phi_{\text{min}}, \qquad (8)$$

where N is a normalization factor; q determines the strength of the bar-like distortion in the equatorial plane;  $q_z$  determines the strength of the bar distortion in the x-z plane; and  $\alpha$ ,  $\beta$ , and  $\gamma$  are exponents whose values are to be determined.  $R_{\rm L2}$  is the distance along the major axis from the center of the bar to its L2 Lagrange point, and  $z_{\rm lim}$  is a vertical scale height. Only values of q,  $q_z$ ,  $z_{\rm lim}$ , and  $R_{\rm L2}$  for which the x-axis coincides with the major axis of the bar will be considered; the y-axis is then the intermediate axis; and the

z-axis is along the bar's minor axis. The angular velocity of the bar and the value of the potential at the center are taken from the numerical Cazes bar, that is  $\Omega=0.5218$  and  $\Phi_{\rm min}=-1.018$ , respectively. When z is set to zero, this potential reduces exactly to the 2D analytical potential that was studied in Barnes & Tohline (2001).

In an effort to illustrate how well the analytical approximation to the Cazes bar potential  $\Phi_{aCB}$ matches the potential that was derived numerically in the Cazes & Tohline (2000) hydrodynamical simulation, Fig. 1 presents equipotential contours from both the numerical Cazes bar and the analytical Cazes bar. Figure 1a shows a slice of the numerical Cazes bar along the positive half of the major axis in the meridional plane. The corresponding slice from the analytical Cazes bar is shown in Fig. 1b. The parameters for the analytical potential pictured here are: N = 0.7, q = 0.8,  $q_z = 1.5, R_{L2} = 1.36, z_{lim} = 0.65, \alpha = 4, \beta = 4,$ and  $\gamma = 1.7$ . Equipotential contours in the y-zplane of the numerical Cazes bar are illustrated in Fig. 1c. Figure 1d displays the corresponding analytical Cazes bar plot. Figures 1e and 1f display equipotential contours in the equatorial planes of the numerical Cazes bar and analytical Cazes bar, respectively. The properties of this equatorialplane, 2D potential were investigated thoroughly in Barnes & Tohline (2001); it will be used below as one of the test potentials. As a check on the applicability of the analytical Cazes bar as a substitute for the numerical Cazes bar, several integrations with identical initial conditions in both potentials have been performed. In every case, the resulting orbital projections had similar (although not exact) morphologies.

# 3. Integration and Characterization Tools

# 3.1. Numerical Orbit Integration

Over the past few decades, numerical integrations of the equations of motion, have become the standard way to investigate stellar orbits in galaxies. In general, the equations of motion have the following vector form,

$$\ddot{\vec{x}} = -\vec{\nabla}\Phi - [\vec{\Omega} \times (\vec{\Omega} \times \vec{x})] - 2\vec{\Omega} \times \dot{\vec{x}}, \qquad (9)$$

where  $\vec{\Omega}$  is the angular velocity of a rotating frame of reference,  $\vec{x}$  is the position vector in that frame,

and  $\Phi$  is the gravitational potential of the system. When a rotating potential is investigated in this paper, the angular velocity vector always points in the z-direction.

Orbits are calculated with a Verlet integration scheme (Verlet 1967). This is straightforward to implement for non-rotating potentials, such as the 2D and 3D Richstone potentials. When a rotating potential is examined, the Verlet scheme is modified so that two Verlet steps are performed per fixed timestep. This is done because Coriolis terms must be included in the accelerations. In order to provide optimum values of velocities for evaluation of the Coriolis terms, a first Verlet step is used to obtain a first estimate of the velocities, but particle positions and velocities are not permanently updated at this step. Then, for the same timestep, the second Verlet step returns and updates a more accurate subsequent position and velocity. This procedure provides an adequate level of energy conservation ( $\Delta \epsilon / \epsilon < 10^{-6}$ over 10<sup>9</sup> timesteps) for the purposes of this investigation. The need for this level of energy conservation is the reason that an analytical formula approximating the Cazes bar potential has been adopted in preference to the original, numerically prescribed  $\Phi_{CB}$ . Using an interpolation scheme with the numerical Cazes bar, the energy error (with the same timestep) is  $\Delta \epsilon / \epsilon \approx 10^{-3}$ . While this is adequate for a determination of the overall shapes of various orbits, the correlation integral method requires that the orbit integration scheme provide much better energy conservation. In principle, the numerical potential could be utilized if a smaller integration timestep were used. In practice, though, this made total integration times too long to be practical. This retreat to an analytical form of the Cazes bar potential should not be taken as a withdrawal from the assertion that the correlation integral method is applicable to numerically derived potentials. On a faster machine (or with an improved interpolation scheme) the computational costs would not have posed as great a problem and a numerical potential could have been used.

Initial conditions for the orbits presented in this paper have not necessarily been chosen to represent a complete sample of phase space. Instead, the orbits discussed here illustrate different (but not all) families that exist in the various potentials. For example, in the Hénon-Heiles potential, two regular and two quasi-ergodic orbits are followed to illustrate their respective differences. Orbits in the 3D analytical Cazes bar potential are populated under the Restriction Hypothesis of Barnes & Tohline (2001). The idea behind the Restriction Hypothesis is that if stars form from gas in a system, the initial velocities of the stars will be determined by the gas flow at the points of formation. In practice, the Restriction Hypothesis is imposed by choosing initial positions that coincide with cylindrical grid points where the gas velocities  $(v_{x,gas}, v_{y,gas}, v_{z,gas})$  from the numerical Cazes bar are known and most definitely does not represent a complete sampling of phase space.

### 3.2. Orbit Morphology

Perhaps the simplest way to categorize any orbit is according to its shape in configuration (x, y, z) space. Examples in 2D potentials are the "banana" orbits discussed in Binney (1982a), the 4/1 orbits described in Contopoulos (1988), and the "bow tie" orbits presented in Barnes & Tohline (2001). For 3D orbits, projections of an orbit onto the three principal planes of the chosen configuration space coordinate system can illustrate the orbital morphology and therefore also can be useful when categorizing orbits. For example, if the x-y plane projection of an orbit appears to have definite circulation about the center (i.e., the zcomponent of the orbital angular momentum,  $L_z$ , is never zero), and the y-z and x-z projections appear as rectangular areas, the orbit is called a z-axis tube orbit (Binney & Tremaine 1987). The benefit of characterizing orbits in this way is that such a descriptive name confers a basic image of the orbit shape that can be recognized in other contexts. The drawbacks to this method are that it is descriptive rather than quantitative; complex orbits usually cannot be simply defined in words; and sometimes the adopted terms are not universally accepted (e.g., Richstone 1982). Another possible problem that arises when dealing with 3D orbits is that, while one planar projection may be simply described, the other two complementary projections may be too complex for words (see, for example, Fig. 9 in Pfenniger 1984). Although orbital morphology will not be used as a primary characterization tool in this paper, orbit projections will be utilized as visual aids when discussing most orbits.

### 3.3. Spectral Dynamics

Another way of classifying 2D and 3D orbits is the spectral dynamics method first introduced to the astrophysical community by Binney & Spergel (1982). Briefly, the spectral dynamics characterization method is based on the fact that regular orbits in near-integrable potentials exist in regions of phase space with toroidal topology. As noted earlier in footnote 1, here the term "regular" means that the number of isolating integrals respected by the orbit is greater than or equal to the dimensionality of the orbital configuration space. These phase space tori can be described in terms of actions and action angles, so the Fourier spectra of the (x(t), y(t), z(t)) components of a regular orbit must consist of discrete lines. The frequencies of these lines are linear combinations of the fundamental frequencies associated with the action angles. The exact linear combinations of frequencies contain information about the resonances of the orbit. Since ergodic and quasi-ergodic orbits do not lie on tori in phase space, their spectra will consist of a forest of lines at all frequencies. For more complete discussions of spectral dynamics, the reader is directed to Binney & Spergel (1982), Laskar (1993), Carpintero & Aguilar (1998), and Copin et al. (2000).

Despite the demonstrated utility of the spectral dynamics method in a variety of contexts, it has not been incorporated into the present study for two reasons. Primarily, the spectral dynamics method does not provide a quantitative measure of quasi-ergodic orbits whereas, as mentioned in the introduction, realistic galactic potentials probably support quasi-ergodic orbits. Secondly, the spectral dynamics method is strictly applicable only to "near-integrable" systems. This means that the Hamiltonian for a given system must be expressible in terms of an integrable part plus some small perturbation. Numerically determined potentials, or their analytical approximations, generally cannot be expected to fall into this category.

# 3.4. Lyapunov Exponents

A more quantitative description of an orbit can be made using Lyapunov exponents. For a given phase space trajectory,  $\vec{\xi}(t) =$  $(x(t), y(t), z(t), p_x(t), p_y(t), p_z(t)),$  the Lyapunov exponents measure how a nearby trajectory,  $\xi(t) + \Delta \xi(t)$ , where  $\Delta \xi$  is initially small, diverges from the given phase space orbit. A number of previous studies of orbits in an astrophysical context have utilized Lyapunov exponents to characterize the orbits. A few examples that contain excellent discussions of the technique are Merritt & Valluri (1996), Habib et al. (1997), and especially Udry & Pfenniger (1988). Briefly, there is one Lyapunov exponent,  $k_i$ , for each dimension i of phase space. In conservative (Hamiltonian) systems (such as all the cases discussed in this paper), these exponents are not independent. In fact,  $\sum_{i} k_{i} = 0$ . Also, the restriction that phase space volumes must remain constant (Liouville's theorem) connects conjugate pairs of exponents. In addition, the exponent that corresponds to motion along the direction of motion is zero. For example, in a 4D phase space two exponents are equal to zero (one is along the direction of motion and the other is in the conjugate direction); the other two exponents are equal in magnitude but have opposite signs (Lichtenberg & Lieberman 1983). In particular, what is measured and referred to as the Lyapunov exponent in this paper is the value of the largest positive exponent. The attractive attributes of this method are its quantitative nature and its applicability to orbits in any potential. The main drawback to using this method as a solo characterization tool is that no distinction can be made between closed and unclosed regular orbits. That is, all regular orbits display insensitivity to small changes in initial conditions and therefore show similar behaviors in their Lyapunov exponents.

The technique for measuring the largest Lyapunov exponent follows from the prescription given in Benettin *et al.* (1976). Lichtenberg & Lieberman (1983) give a good introduction to the method, starting from the definition of the Lyapunov exponent, which is summarized here. The assumption is made that two nearby trajectories diverge exponentially with time, i.e.,

$$d(t) = d(0)e^{kt}, (10)$$

where d denotes a phase space distance. The Lyapunov exponent can then be defined to be,

$$k \equiv \lim_{t \to \infty, d(0) \to 0} \left(\frac{1}{t}\right) \ln \left[\frac{d(t)}{d(0)}\right]. \tag{11}$$

If a chosen orbit is quasi-ergodic, so that two nearby trajectories diverge as  $e^{\sigma t}$ , then  $k = \sigma =$  constant. If, instead, the chosen orbit is regular and nearby trajectories diverge only as a power law in time,  $d(t) \sim d(0)t^{\alpha}$ , then

$$k = -\frac{\alpha}{t} \ln t. \tag{12}$$

In this case, a plot of  $\ln k$  vs.  $\ln t$  should have a slope  $\approx -1$  for large values of t, independent of the precise value of the exponent  $\alpha$ .

The definition of k as given in eq.(11) is computationally unsatisfactory. Exponential growth can quickly lead to numbers that a computer cannot represent. Benettin  $et\ al.\ (1976)$  suggest, instead, that an orbit be broken into n finite time lengths,  $\tau$  (see their Fig. 1 or Fig. 5.6 in Lichtenberg & Lieberman 1983 for a pictoral representation of this idea). Then, every  $\tau$  time units, the distance between neighboring trajectories should be re-normalized to the distance between the two at the beginning of the orbit. With this technique, the Lyapunov exponent is defined to be (Benettin  $et\ al.\ 1976$ ),

$$k_n = \frac{1}{n\tau} \sum_{i=1}^n \ln \frac{d(i\tau)}{d(0)},\tag{13}$$

where, in the limit of  $n \to \infty$ ,  $k_n \to k$ .

The task that remains is to calculate whether or not nearby trajectories exponentially diverge. The vector of interest here is  $\vec{\Delta\xi}$ , that is, the vector difference between the orbit that is integrated and the nearby trajectory. Following Lichtenberg & Lieberman (1983), define  $\vec{w} \equiv \vec{\Delta\xi}$ . From a linear stability analysis (as in Binney & Tremaine 1987, §3.5.3), then,

$$\frac{d\vec{w}}{dt} = \mathcal{M} \cdot \vec{w},\tag{14}$$

and  $\mathcal{M}$  is a tensor that has components defined by,

$$\mathcal{M} \equiv \frac{\partial \vec{F}}{\partial \vec{\xi}},\tag{15}$$

where  $\vec{F} = \left(-\frac{\partial H}{\partial \vec{x}}, \frac{\partial H}{\partial \vec{p}}\right)$ , H is the system's Hamiltonian,  $\vec{x}$  is the generalized coordinate vector, and

 $\vec{p}$  is the conjugate momentum vector. In a system with N degrees of freedom, there are now 3N equations that must be solved – N for the particle trajectory and 2N for the phase space difference vector.

The 2N differential equations given by eq.(14) are translated into finite-difference equations that are solved alongside the equations of motion. For orbits that will be analyzed in this paper,  $k_n$  is determined for  $n\tau = 10^2$ ,  $5 \times 10^2$ ,  $10^3$ ,  $5 \times 10^3$ , and  $10^4$ . In addition, the value of  $\tau$  has been chosen to be the same as  $\Delta t$ , so the difference vector is renormalized every timestep. The presentation of Lyapunov exponents is in the form of plots showing  $\ln k_n$  versus  $\ln n\tau$ . This form has been chosen for these plots because regular orbits (those insensitive to small changes in initial conditions) have slopes  $\approx -1$ , while quasi-ergodic orbits have slopes  $\approx 0$  because they are sensitive to initial conditions.

### 3.5. Correlation Integrals

The main orbital characterization method that will be utilized in this paper is the correlation integral method. As described by Grassberger & Procaccia (1983a) and Carnevali & Santangelo (1984), the correlation integral provides a measurement of phase space dimensionality. The basic idea underlying this method is that for a given orbit, the correlation integral is calculated for all phase space. Then, since a plot of the correlation integral versus phase space distance behaves like a power law for small phase space distances (Grassberger & Procaccia 1983a), the exponent of the power law provides a measure of the dimensionality of the phase space that is occupied by the orbit. Once this dimensionality is known, one can also readily deduce the number of isolating integrals that are respected by the selected orbit. Approaching a previously unexamined potential in this way gives, for example, basic information about whether or not most orbits are regular. This characterization then may or may not lead one to perform a more complex analysis, such as spectral dynamics.

Operationally, the steps in determining the dimensionality of a phase space orbit are:

1. Integrate an orbit for a sufficient number of timesteps ("sufficient" will be clarified below).

- Choose a set of sampling points from the orbit.
- 3. Calculate the correlation integral, C(r), as defined by eq. (16).
- 4. Measure a slope from a plot of  $\ln C(r)$  vs.  $\ln r$ .

Because topics 1 and 2 are somewhat connected, they are discussed together. From various trials, investigating phase spaces of different sizes, it has been determined that approximately 50 orbital periods must be completed in order for an accurate correlation integral to be found. This means that more timesteps are necessary for each 3D orbit than for each 2D orbit. With the timestep that has been used throughout this investigation, the ratio between the number of required timesteps is  $\approx 100$ . (It is likely that these numbers would change if a different integration scheme was used.) The sampling points are chosen following the suggestion in Carnevali & Santangelo (1984); specifically, random points are selected from a subset of the orbital phase space points. The subset consists of 10<sup>5</sup> points taken at equal timestep intervals. Normally, 10% of these points are randomly chosen to be sampling points. While this number of sampling points is usually adequate for the purposes of this study, it generally is best to use as many sampling points as is computationally practical.

The correlation integral is determined numerically using the following formula (Grassberger & Procaccia 1983a):

$$C(r) = \lim_{N \to \infty} \frac{1}{N^2} \sum_{i=1}^{N} \sum_{j=1, \neq i}^{N} \Theta(r - |\vec{\xi_i} - \vec{\xi_j}|), (16)$$

where  $\Theta$  is the Heaviside step function, the  $\xi_i$  are phase space position vectors, r is a phase space distance, and N is the number of sampling points from the orbit. It is now clear why it is advisable to use as large a value of N as practical, as the correlation integral is defined more accurately when N is larger. A naive evaluation of eq.(16) is very slow for large N, even if one takes advantage of the symmetry of the Heaviside function. Dividing phase space into "bins" can significantly speed up the evaluation of the double summation.

The final step in determining the dimensionality of a phase space orbit is measuring a slope from

the plot of  $\ln C(r)$  vs.  $\ln r$ . A log-log plot is used because of the behavior of the correlation integral. Grassberger & Procaccia (1983a) state that, for  $r \ll 1, C(r) \propto r^{\nu}$ , where  $\nu$  is the dimensionality of the phase space orbit. So, when  $\ln C(r)$  is plotted against  $\ln r$ , the slope of any linear section can be interpreted as the dimensionality  $\nu$  of the phase space orbit within that range of r. In order to ascertain the reliability of the values of  $\nu$  that have been measured for individual orbits, a minimized  $\chi^2$  linear fit to the  $\ln C(r) - \ln(r)$  data for five independent sets of sampling points has also been calculated. Also, at least one order of magnitude in r must be covered by the linear section to be considered. It is the average slopes  $(D = \langle \nu \rangle)$  and standard deviations  $(\sigma)$  of these five linear fits that are reported in the legends of figures such as Fig. 11b.

#### 4. Results

The individual phase space orbits that are discussed in this section are listed in Table 1. As indicated in the first column of Table 1, the orbits are identified by the potential (or mapping) in which they exist. Listed in column 2 are the corresponding figure numbers that contain visual summaries of the orbital analysis. The initial conditions (positions, velocities, and energies) for each of the orbits are listed in the next seven columns. The last two columns of Table 1 are provided as a quick reference to the Lyapunov exponent and correlation integral characterizations that have been determined for each orbit. If the next to last column (labeled Lyapunov) contains an 'I' (denoting an orbit insensitive to small changes in initial conditions), that orbit is regular; an 'S' (for sensitive) denotes an orbit that is not regular. The last column holds the measured dimensionality D of each phase space orbit.

Before undertaking a discussion of the characterization of these selected orbits, let us examine the expectations for the various models. The 2D phase space of the Hénon map is not derived from a Hamiltonian system, so there are no integrals of motion for this system per se. However, each of the 4D phase spaces (2D Richstone, Hénon-Heiles, and 2D Cazes bar) is a Hamiltonian system. In these cases, the potentials are time-invariant so the energy (or  $\epsilon_J$ ) must be an integral, and we

should find that  $D \leq 3$  for all orbits. Fully ergodic orbits will have D=3, while quasi-ergodic orbits will have 2 < D < 3. Quasi-ergodic orbits respect only one full integral of motion, but they also have some (unknown) restriction in addition to that of their ergodic cousins. Both ergodic and quasi-ergodic orbits are sensitive to initial conditions, so the Lyapunov exponent should remain nearly constant with time, as discussed in §3.4. On the other hand, a regular orbit must have a total number of isolating integrals that is equal to or greater than the number of spatial degrees of freedom (in this case  $\geq 2$ ; specific energy plus 1 or 2 unknown integrals). So, the allowed phase space for each regular (but not periodic) orbit should be 2D (4 phase space dimensions minus the 2 isolating integral dimensions). The behavior of the Lyapunov exponent should be that of a regular orbit, that is, the slope of  $\ln k_n$  vs.  $\ln n\tau$  should be  $\approx -1$ .

Orbits in 3D Hamiltonian systems occupy 6D phase spaces. However, since the potentials are still time-invariant, the measured dimensionality of the phase space orbit should be, at most, five. Regular orbits in 3D potentials must respect at least three integrals of motion,  $D \leq 3$ , and as before, the Lyapunov exponent should decrease with time for a regular orbit. Returning to the nonregular orbits, fully ergodic orbits should display a dimensionality D = 5, while quasi-ergodic orbits should have a noninteger value 4 < D < 5. Orbits with 3 < D < 4 are neither regular nor quasiergodic. They respect (at least) two full integrals of motion and will be referred to as semiregular orbits in this paper. All nonregular orbits have Lyapunov exponent plots that have  $\ln k_n$  vs.  $\ln n\tau$ slopes that are  $\approx 0$ .

### 4.1. 2D Phase Space

As mentioned earlier, the Hénon map phase space is fractal (see §2.1). The accepted value for the dimensionality of this phase space orbit is  $D=1.25\pm0.02$  (Grassberger & Procaccia 1983a). Figure 2a shows the (x,y) phase space structure of the Hénon map; Fig. 2b is a magnified view illustrating the fractal nature of this phase space orbit. Figure 2c shows the  $\ln C(r)$  vs.  $\ln r$  plot (hereafter, the C-r plot) that was obtained in this study for the Hénon map using the correlation

integral method. The result is  $D = 1.21 \pm 0.01$ . This is also the value that Grassberger & Procaccia (1983a) obtained using the correlation integral method. The difference between this result and the accepted value is discussed in Grassberger & Procaccia (1983b). They claim that there is a systematic error in the determination of the Hénon map correlation integral. Interestingly, this error does not occur in correlation integral determinations for other maps such as the Kaplan-Yorke map, the logistic equation, or the Lorenz equation (Grassberger & Procaccia 1983b). They conclude that the error in the Hénon map result arises from the sample phase space points not uniformly covering the phase space orbit. However, their suggested remedy does not work well when phase space is populated by numerically integrated orbits. In the following sections it will be shown that this slight disagreement does not diminish the quantitative usefulness of the correlation integral method as a tool for characterizing orbits.

### 4.2. 4D Phase Space

For orbits in 2D potentials, the presentation of results will adhere to the following form: In each figure, the frame labeled (a) contains the orbital trajectory; frame (b) displays the C-r plot obtained using the correlation integral method; frame (c) shows the Lyapunov exponent plot as  $\ln k_n$  vs.  $\ln n\tau$ ; and frame (d) contains either the  $(x-p_x)$  or  $(R-p_R)$  surface of section diagram for the orbit. The legends of frames labeled (b) also will provide quantitative information derived from the C-r plot as discussed in §3.5, namely the slope D and standard deviation  $\sigma$ . In most Lyapunov exponent plots, a dot-dashed line with a slope of -1 also is included because, as discussed in §3.4, the behavior of  $k_n$  should approach this slope as  $n\tau \to \infty$  if an orbit is regular.

The results for four orbits in the 2D Richstone potential are shown in Figs. 3 through 6. In every case, all three techniques for characterizing the orbits indicate that the orbits are regular: the surface of section plots are composed of invariant curves; the Lyapunov exponent drops with time with a slope of minus one; and from the correlation integral, the measured dimensionality has a value  $\leq 2$ . Note that the Lyapunov exponent plots in Figs. 3c and 6c are basically identical and

therefore make no distinction between the closed and unclosed regular orbits. However, the difference is clearly illustrated by the differing slopes of the C-r plots in Figs. 3b and 6b: the periodic orbit displays D=1, instead of D=2.

At this point, it is worth noting some general features of C-r plots derived from orbits (of any dimensionality) as opposed to mappings. As the value of r increases, the plotted points will often deviate from the line of slope D. This is because a clean linear relation is expected only for  $r \ll 1$ . Another way to think about this is that, for a sufficiently large value of phase space distance  $r_0$ , the entire phase space orbit will be enclosed. Then, for  $r \geq r_0$ , C(r) = 1.0, so the C - r plot must tend toward a slope of zero at large enough values of r. Deviations from a linear slope of Dmay also occur at the smallest values of r, but for a different reason. Since only a finite number of sampling points is used, there is necessarily a lower limit to the smallest distance that can be measured between any two points. Basically, this is a small-number statistics problem. As a larger number of sampling points is used, the linear fit generally becomes tighter and extends to smaller values of r.

Four orbits with  $\epsilon = 1/8$  in the Hénon-Heiles potential are displayed and analyzed in Figs. 7 through 10. Unlike the 2D Richstone potential, the Hénon-Heiles potential supports some quasiergodic orbits at this energy. All three methods of characterization indicate that the orbits shown in Figs. 7 and 8 are regular, while the ones shown in Figs. 9 and 10 are quasi-ergodic. Focusing on the two quasi-ergodic orbits, notice that, (1) the Lyapunov exponent is approximately constant, signaling an exponential departure of two initially neighboring trajectories; (2) the surface of section is no longer composed of a smooth invariant curve; and (3) the C-r plot identifies a dimension greater than two. We know that the orbits shown in Figs. 9 and 10 are quasi-ergodic rather than fully ergodic because of the measured dimensionality. This is a distinction that can be made clearly from the C-r plot, but it is not possible from a measurement of the Lyapunov exponent alone. The deviations from D at small values of rin Figs. 9b and 10b are simply artifacts of the limited number of orbital timesteps. This is similar to the small number statistics problem that was discussed above. When the number of timesteps is increased, these deviations disappear and the line with slope D extends to smaller r values.

Four different orbits that are supported by the 2D analytical Cazes bar potential are presented here in Figs. 11 through 14. Once again, all three methods of characterizing these 2D orbits agree: the orbits shown in Figs. 11, 12, and 13 are regular, while the one shown in Fig. 14 is quasiergodic. The orbit shown in Fig. 11a has  $D \approx 1$ , rather than D=2; hence, it is periodic. This orbit is the parent of what has been called the 'bow tie' family of orbits in Barnes & Tohline (2001). The orbit shown in Fig. 12a appears to be trapped near the periodic bow tie orbit. The most interesting aspect of this orbit is visible in the C-r plot, Fig. 12b. There are two linear sections in the C-rplot. The one that exists for small r has a slope of  $D \approx 2$ . At larger r, however, the linear section has a slope of  $D \approx 1$ . This slope discontinuity persists even when this orbit is followed through 100 times as many timesteps. This suggests that the discontinuity and the r location of the discontinuity are physically relevant (as opposed to the cases in the previous paragraph where differing slopes were numerical artifacts). We interpret this difference using the following analogy presented by Gleick (1987). Imagine viewing a ball of string from very far away. If asked to describe the dimensionality of the ball of string, which appears to be a point, the answer would be zero. Moving closer, the ball can be seen to be extended. The ball now appears to have dimensionality equal to 2. Moving even closer, the ball now appears to have a finite extent in a direction perpendicular to the dimensions already present as well, and is thus a 3D object. However, observing the ball of string at very close range, the one-dimensional nature of the string becomes apparent. So, the dimensionality of the phase space orbit can change depending on what length scale is observed. Indeed, for small enough values of r, all phase space orbits derived from particle trajectories are really 1D objects. With this in mind, the segment with slope  $D \approx 1$  is interpreted as demonstrating that the orbit is not far from being closed. The r value at which the change in slope occurs identifies a critical length scale for this orbit that cannot be determined via the Lyapunov exponent method or from surfaces of section.

The quasi-ergodic orbit shown in Fig. 14 has a dimensionality  $D \approx 2.54$ . Unlike the discontinuity present in the regular orbit C-r plot (Fig. 12b), the apparently linear slope at smaller r values is dependent on the number of timesteps taken for the orbit, as with the orbits shown in Figs. 9 and 10.

## 4.3. 6D Phase Space

As with the 2D orbits previously discussed, the figures containing results for individual 3D orbits all have a similar form. Each figure consists of: a frame labeled (a) illustrating the x-y projection of the orbit; a frame labeled (b) illustrating the x-z orbital projection; a frame labeled (c) illustrating the y-z projection of the orbit; a frame (d) showing the C-r plot for the orbit; and finally, a frame labeled (e) that displays the Lyapunov exponent plot derived from the orbit.

Figures 15 through 17 display results for three different orbits in the 3D Richstone potential. As expected, these results support the characterization of these orbits as regular. In this case, the three integrals of motion are the energy, the z-component of angular momentum (which was explicitly conserved in the 2D case), and the unknown integral that was also apparent in the 2D case. These figures demonstrate that the correlation integral method agrees with other characterization techniques for 3D as well as 2D orbits.

While it has been important to use individual orbits to compare characterization methods, it is useful to investigate ensembles of orbits using only correlation integrals. As stated in §2.4, Stäckel potentials provide an excellent test bed for characterization methods. One hundred orbits of varying energies (25 orbits each at E=-0.2, -0.4, -0.6, -0.8) have been integrated in the potential given by eq. (7). These orbits have zero initial velocities and initial positions that cover one octant of the given energy surface.

The results are shown in Fig. 18. This histogram shows the number of orbits versus the number of integrals of motion respected by those orbits. Note that the number of integrals of motion I is determined by subtracting the D value taken from a C-r plot from the phase space dimension. In this case, I=6-D. There is some scatter about the expected value of I=3.

This scatter is due to the fact that only 10,000 sampling points have been used. For example, the orbit that here appears to respect only 2.6 integrals of motion gives a value of 3 when 10 times as many sampling points are used. However, this improved accuracy comes at the price of computing time. Ten times as many sampling points means an increase by a factor of 100 in computing time (from about 7 minutes to about 12 hours per orbit). This made it impractical to use more sampling points for each of the 100 orbits. Despite this scatter, the majority (81%) of the results lie between 2.8 and 3.1. The small cluster of orbits that respect 4 integrals of motion are those confined to symmetry planes of the potential.

Another histogram of an ensemble of 100 orbits is shown in Fig. 19. These orbits are supported by the 3D analytical Cazes bar potential and, like orbits in the Stäckel potential, there are four groups of 25 orbits at different energies ( $\epsilon_J = -0.96$ , -0.85, -0.75, -0.63). The initial positions of these orbits have been chosen to cover one quarter of the given energy surface. The initial velocities of these orbits have been specified by the Restriction Hypothesis discussed in §3.1.

The most conspicuous feature of this histogram is that the integrals of motion are not concentrated around a single value. What this histogram shows is that the 3D Cazes bar potential supports orbits that respect 3 integrals of motion (regular), 2 integrals of motion (semiregular), and 1 integral of motion (quasi-ergodic). While this histogram has not been created with a self-consistent stellar distribution (which is a future project), it does give the flavor of how such a distribution will appear. Additionally, histograms of the 25 orbits at the various Jacobi constants are also interesting. They show a trend for an increasing fraction of nonregular orbits with increasing energy. This is similar to the trend for orbits in the Hénon-Heiles potential.

### 5. Discussion & Conclusions

Building on the work of Grassberger & Procaccia (1983a) and Carnevali & Santangelo (1984), a flexible technique for characterizing orbits in 3D potentials known as the correlation integral method has been presented. This method analyzes phase space orbits and returns a single num-

ber, the dimensionality of the phase space orbit. From this number and the dimensionality of the underlying phase space, the number of isolating integrals of motion respected by an orbit can be determined. This number can then be used as a quantitative characterization attribute.

The implementation of the correlation integral method has been tested for a variety of previously studied systems. More familiar characterization tools, such as surfaces of section and Lyapunov exponents, support the results obtained with the correlation integral method. The advantages of the correlation integral are most apparent when used to characterize orbits in 3D potentials. A unique, 3D potential based on a numerically created potential-density pair called the Cazes bar has been presented. The Cazes bar is rotating and has no geometrical symmetries that give rise to analytical integrals of motion. However, the correlation integral method demonstrates that regular orbits exist in the Cazes bar potential. Additionally, the correlation integral method distinguishes between orbits that respect two integrals of motion and those that respect only one integral.

The simple fact that the correlation integral method can reproduce the results of other characterization methods is not enough to warrant its adoption. Here the various categorizing methods discussed in this paper are compared and contrasted.

- When analyzing orbits in a 4D phase space, surface of section diagrams are the simplest and clearest way to characterize orbits. However, there is no simple quantitative measure that describes quasi-ergodic orbits in surface of section diagrams. Also, these diagrams are not easily translated to 6D phase spaces. The correlation integral method addresses both of these problems.
- Lyapunov exponents provide quantitative measures of orbital regularity in arbitrary 2D and 3D potentials. Unfortunately, all regular orbits, closed and unclosed, share the same signature in Lyapunov exponent plots. For orbits in 3D potentials, the behavior of the Lyapunov exponent is also the same for all nonregular orbits. That is, no distinction is made between orbits that respect only one integral of motion and those

that respect two. The correlation integral method distinguishes between these types of regular (periodic and unclosed) and nonregular (respecting only one or two integrals of motion) orbits.

• The spectral dynamics characterization method rests on the assumption that the potential being investigated is at least nearintegrable. When this is true, the spectral dynamics method provides an excellent way to analyze orbits. If, instead, the potential is the result of a numerical simulation or is not clearly near-integrable, then spectral dynamics may not give relevant results. Also, spectral dynamics only returns information about regular orbits. If it is true that quasi-ergodic orbits play a role in galactic structure, then it will be necessary to utilize a characterization tool, such as the correlation integral method, that incorporates those orbits.

The correlation integral method could prove useful for a variety of future studies, but there are two particular avenues of interest. Investigations of the impact of massive central objects on stellar orbits could benefit from the correlation integral method in the following way. By creating histograms, like those shown here in Figs. 18 and 19, from orbits in potentials with point masses, the general characteristics of such a stellar system can be seen. This information may prove useful when creating self-consistent stellar distribution functions to describe black hole/stellar systems (e.g., van der Marel et al. 1998, Gebhardt et al. 2000b).

The correlation integral method also should be a good way to analyze stellar orbits in cosmological simulations that include star formation. By simply keeping a record of the phase space coordinates of all stars during a simulation, the correlation integral method can be used to analyze the stellar distribution functions in the emerging potentials. To use the Lyapunov exponent method, extra equations would need to be solved during an already complex calculation. Similarly, the spectral dynamics technique may not be expedient if the potentials that arise are not sufficiently close to integrable forms.

In conclusion, the correlation integral method

is a flexible, quantitative, and straightforward way of characterizing orbits in 3D potentials. It is recommended that it be broadly adopted as a tool for characterizing the properties of orbits in all Hamiltonian dynamical systems. However, there are three specific cases of astrophysical interest to which the correlation integral method seems particularly well suited: analyzing stellar distribution functions in analytically and numerically specified models of steady-state galactic potentials (especially those with Hamiltonian chaos); investigating the orbital structure supported by galactic potentials formed in cosmological simulations; and quantifying the response of stellar systems to potentials that contain central point masses.

The author would like to thank Joel Tohline, Dana Browne, and Hal Levison for providing valuable insight on the topics presented here. This work has been supported, in part, by funding from the US National Science Foundation through grant AST 99-87344. Additional support has been provided by the Louisiana Board of Regents' LEQSF under agreement LEQSF(1996-01)-GF-08 and through NASA/LaSPACE under grant NGT5-40035. This work also has been supported, in part, by grants of high-performance computing time through NPACI machines at the San Diego Supercomputer Center.

#### REFERENCES

Barnes, E., & Tohline, J. 2001, ApJ, 551, 80

Benettin, G., Galgani, L., & Strelcyn, J. 1976, Phys. Rev. A, 14, 2338

Binney, J. 1981, MNRAS, 196, 455

Binney, J. 1982a, MNRAS, 201, 1

Binney, J. 1982b, MNRAS, 201, 15

Binney, J., & Spergel, D. 1982, ApJ, 252, 308

Binney, J., & Tremaine, S. 1987, Galactic Dynamics, (Princeton: Princeton Univ. Press)

Carnevali, P., & Santangelo, P. 1984, ApJ, 281, 473

Carpintero, D., & Aguilar, L. 1998, MNRAS, 298,

7

TABLE 1
ORBIT INFORMATION

Orbit	Fig. #	$x_0$	$y_0$	$z_0$	$\dot{x_0}$	$\dot{y_0}$	$\dot{z_0}$	$\epsilon$ or $\epsilon_J$	Lyapunov <sup>a</sup>	D
Hénon map	2	0.0	0.0							1.21
2D Richstone #1	3	0.5	0.0		0.0	0.4		-0.574	I	2
2D Richstone #2	4	0.5	0.0		0.2	0.2		-0.614	I	2
2D Richstone #3	5	0.5	0.0		1.12	0.23		0.0	I	2
2D Richstone #4	6	0.136	-0.532		0.0	0.0		-4.56(-2)	I	1
Hénon-Heiles #1	7	0.0	0.3		0.422	0.0		0.125	I	1
Hénon-Heiles #2	8	0.0	0.14		0.481	0.0		0.125	I	2
Hénon-Heiles #3	9	0.0	0.24		0.402	0.2		0.125	$\mathbf{S}$	2.4
Hénon-Heiles #4	10	0.0	0.24		0.281	0.35		0.125	$\mathbf{S}$	2.3
2D Cazes bar #1	11	0.67	0.0		0.0	0.611		-0.75	I	1
2D Cazes bar #2	12	0.65	0.0		0.0	0.628		-0.75	I	2
2D Cazes bar #3	13	0.5	0.0		0.0	0.712		-0.75	I	2
2D Cazes bar #4	14	0.5	-0.5		0.0	0.507		-0.75	$\mathbf{S}$	2.5
3D Richstone #1	15	0.5	0.0	0.0	0.4	0.4	0.7	-0.269	I	3
3D Richstone #2	16	0.6	0.0	0.2	0.5	0.2	-0.05	-0.263	I	3
3D Richstone #3	17	0.5	0.0	0.3	0.4	0.5	0.01	-0.229	I	3

<sup>&</sup>lt;sup>a</sup>The letters that appear in this column distinguish between orbits that are insensitive (I) to small changes in initial conditions and those that are sensitive (S) to such changes. All orbits labeled 'I' are regular.

- Carpintero, D., Muzzio, J., & Wachlin, F. 1999, CeMDA, 73, 159
- Cazes, J. 1999, Ph.D. thesis, Louisiana State University
- Cazes, J., & Tohline, J. 2000, ApJ, 532, 1051
- Colpi, M., Mayer, L., & Governato, F. 1999, ApJ, 525, 720
- Combes, F., & Sanders, R. 1981, A&A, 96, 164
- Contopoulos, G., & Papayannopoulos, Th. 1980, A&A, 92, 33
- Contopoulos, G. 1988, A&A, 201, 44
- Copin, Y., Zhao, H., & de Zeeuw, P. 2000, MN-RAS, 318, 781
- Cretton, N., de Zeeuw, P., van der Marel, R., & Rix, H-W. 1999, ApJS, 124, 383
- Cretton, N., Rix, H-W., & de Zeeuw, P. 2000, ApJ, 536, 319
- de Zeeuw, P., & Lynden-Bell, D. 1985, MNRAS, 215, 713
- Ferrarese, L., & Merritt, D. 2000, ApJ, 539, L9
- Gebhardt, K., et al. 2000a, ApJ, 539, L13
- Gebhardt, K., et al. 2000b, ApJ, 543, L5
- Gerhard, O., & Binney, J. 1985, MNRAS, 216, 467
- Gleick, J. 1987, Chaos: Making a New Science, (New York: Penguin)
- Goodman, J., & Schwarzschild, M. 1981, ApJ, 245, 1087
- Grassberger, P., & Procaccia, I. 1983, Phys. Rev. Lett., 50, 346
- Grassberger, P., & Procaccia, I. 1983, Physica, 9D, 189
- Habib, S., Kandrup, H., & Mahon, M. 1997, ApJ, 480, 155
- Hasan, H., Pfenniger, D., & Norman, C. 1993, ApJ, 409, 91
- Heisler, J., Merritt, D., & Schwarzschild, M. 1982, ApJ, 258, 490

- Hénon, M. 1976, Comm. Math. Phys., 50, 69
- Hènon, M., & Heiles, C. 1964, AJ, 69, 73
- Hohl, F., & Zang, T. 1979, AJ, 84, 585
- Kalnajs, A. 1976, ApJ, 205, 751
- King, I. 1966, AJ, 71, 64
- Laskar, J. 1993, CeMDA, 56, 191
- Lichtenberg, A., & Lieberman, M. 1983, Regular and Stochastic Motion, (New York: Springer-Verlag)
- Lütticke, R., Dettmar, R.-J., & Pohlen, M., 2000a, A&AS, 145, 405
- Lütticke, R., Dettmar, R.-J., & Pohlen, M., 2000b, A&A, 362, 435
- Magnenat, P. 1982, A&A, 108, 89
- Martinet, L., & de Zeeuw, T. 1988, A&A, 206, 269
- Merritt, D., & Valluri, M. 1996, ApJ, 471, 82
- Mulder, W., & Hooimeyer, J. 1984, A&A, 134, 158
- Miller, R., & Smith, B. 1979, ApJ, 227, 785
- Miller, R., Vandervoort, P., Welty, D., & Smith, B. 1982, ApJ, 259, 559
- Pfenniger, D. 1984, A&A, 134, 373
- Pfenniger, D., & Friedli, D. 1991, A&A, 252, 75
- Pilat-Lohinger, E., Dvorak, R., & Burger, Ch. 1999, CeMDA, 73, 117
- Richstone, D. 1980, ApJ, 238, 103
- Richstone, D. 1982, ApJ, 252, 496
- Rix, H-W., de Zeeuw, P., Cretton, N., van der Marel, R., & Carollo, C. 1997, ApJ, 488, 702
- Schwarzschild, M. 1979, ApJ, 232, 236
- Schwarzschild, M. 1982, ApJ, 263, 599
- Sparke, L., & Sellwood, J. 1987, MNRAS, 225, 653
- Udry, S., & Pfenniger, D. 1988, A&A, 198, 135
- Valluri, M., & Merritt, D. 1998, ApJ, 506, 686

van der Marel, R., Cretton, N., de Zeeuw, P., & Rix, H-W. 1998, ApJ, 493, 613

Verlet, L. 1967, Phys. Rev., 159, 98

Williams, H., & Tohline, J. 1987, ApJ, 315, 594

Fig. 2.— Hénon map. (a) Plot of phase space points obtained after 100,000 iterations of eqs. (2) and (3). (b) Magnification of the plot in (a). The small scale substructure is a telltale sign of the fractal nature of the phase space orbit. (c) A plot of the correlation integral  $(\ln C(r))$  versus phase space distance  $(\ln r)$  for this mapping. The value of D shown in the legend has been measured from the slope of the line;  $\sigma$  is the standard deviation measured for D, as described in §3.5.

Fig. 3.— Orbit #1 in the 2D Richstone potential; see Table 1 for initial conditions. (a) The R-z trajectory of this orbit. (b) The associated C-r plot listing the average slope (D) and standard deviation  $(\sigma)$ . (c) The plot of the Lyapunov exponent  $(\ln k_n)$  versus integration time  $(\ln n\tau)$  for this orbit. (d) The  $(R-p_R)$  surface of section for this orbit.

Fig. 4.— Orbit #2 in the 2D Richstone potential; each frame contains information as described in the caption to Fig. 3.

Fig. 6.— Orbit #4 in the 2D Richstone potential; each frame contains information as described in the caption to Fig. 3.

This 2-column preprint was prepared with the AAS IATEX macros v5.0.

Fig. 1.— (a) Equipotential contours of the numerical Cazes bar in the x-z plane for x>0; (b) equipotential contours of the analytical Cazes bar in the same plane. (c) Equipotential contours of the numerical Cazes bar in the y-z plane for y>0; (d) equipotential contours of the analytical Cazes bar in the same plane. (e) Equipotential contours of the numerical Cazes bar in the x-y plane; (f) equipotential contours of the analytical Cazes bar in the same plane.

Fig. 5.— Orbit #3 in the 2D Richstone potential; each frame contains information as described in the caption to Fig. 3.

Fig. 7.— Orbit #1 in the Hénon-Heiles potential; see Table 1 for initial conditions. (a) The R-z trajectory of this orbit. (b) The associated C-r plot listing the average slope (D) and standard deviation  $(\sigma)$ . (c) The plot of the Lyapunov exponent  $(\ln k_n)$  versus integration time  $(\ln n\tau)$  for this orbit. (d) The  $(R-p_R)$  surface of section for this orbit.

Fig. 8.— Orbit #2 in the Hénon-Heiles potential; each frame contains information as described in the caption to Fig. 7.

Fig. 9.— Orbit #3 in the Hénon-Heiles potential; each frame contains information as described in the caption to Fig. 7.

Fig. 10.— Orbit #4 in the Hénon-Heiles potential; each frame contains information as described in the caption to Fig. 7.

Fig. 11.— Orbit #1 in the 2D Cazes bar potential; see Table 1 for initial conditions. (a) The x-y trajectory of this orbit. (b) The associated C-r plot listing the average slope (D) and standard deviation  $(\sigma)$ . (c) The plot of the Lyapunov exponent  $(\ln k_n)$  versus integration time  $(\ln n\tau)$  for this orbit. (d) The  $(x-p_x)$  surface of section for this orbit.

Fig. 12.— Orbit #2 in the 2D Cazes bar potential; each frame contains information as described in the caption to Fig. 11.

Fig. 13.— Orbit #3 in the 2D Cazes bar potential; each frame contains information as described in the caption to Fig. 11.

Fig. 14.— Orbit #4 in the 2D Cazes bar potential; each frame contains information as described in the caption to Fig. 11.

Fig. 15.— Orbit #1 in the 3D Richstone potential; see Table 1 for initial conditions. (a) The x-y plane projection of this orbit. (b) The x-z plane projection of the same orbit. (c) The y-z plane projection of the same orbit. (d) The associated C-r plot listing the average slope (D) and standard deviation  $(\sigma)$ . (e) The plot of the Lyapunov exponent  $(\ln k_n)$  versus integration time  $(\ln n\tau)$  for this orbit.

Fig. 16.— Orbit #2 in the 3D Richstone potential; each frame contains information as described in the caption to Fig. 15.

Fig. 17.— Orbit #3 in the 3D Richstone potential; each frame contains information as described in the caption to Fig. 15.

Fig. 18.— Histogram of the number of orbits versus the number of integrals of motion for 100 orbits in the Stäckel potential described in §2.4.

Fig. 19.— Histogram of the number of orbits versus the number of integrals of motion for 100 orbits in the 3D analytical Cazes bar potential.

This figure "f1.gif" is available in "gif" format from:

This figure "f2.gif" is available in "gif" format from:

This figure "f3.gif" is available in "gif" format from:

This figure "f4.gif" is available in "gif" format from:

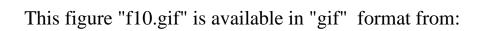
This figure "f5.gif" is available in "gif" format from:



This figure "f7.gif" is available in "gif" format from:

This figure "f8.gif" is available in "gif" format from:

This figure "f9.gif" is available in "gif" format from:



This figure "f11.gif" is available in "gif" format from:

This figure "f12.gif" is available in "gif" format from:

This figure "f13.gif" is available in "gif" format from:

This figure "f14.gif" is available in "gif" format from:

This figure "f15.gif" is available in "gif" format from:



This figure "f17.gif" is available in "gif" format from:

This figure "f18.gif" is available in "gif" format from:

This figure "f19.gif" is available in "gif" format from: